Pile penetration in crushable soils

Ciantia, Matteo; O'Sullivan, C.; Jardine, Richard J.

Published in:
Proceedings of the XVII ECSMGE-2019

DOI:
10.32075/17ECSMGE-2019-1111

Publication date:
2019

Document Version
Publisher's PDF, also known as Version of record

Proceedings of the XVII ECSMGE-2019
Geotechnical Engineering foundation of the future
ISBN 978-9935-9436-1-3

doi: 10.32075/17ECSMGE-2019-1111

XVII European Conference
ECSMGE 2019
Reykjavik
on Soil Mechanics
and Geotechnical Engineering

Pile penetration in crushable soils: Insights from micromechanical modelling

Pénétration des pieux dans les sols concassables: informations tirées de la modélisation micromécanique

M. O. Ciantia
University of Dundee, School of Science and Engineering, Dundee, UK

C. O'Sullivan and R. J. Jardine
Imperial College, Dept. Civil and Environmental Engineering, London, UK

ABSTRACT: A 3D discrete element model (DEM) was used to simulate calibration chamber experiments of a cone shaped tip pile penetrating into crushable granular media. Both monotonic and cyclic jacking are considered. Particle crushing is simulated by employing a rigorous breakage criterion applied to elasto-brittle spheres. Particle scaling is used to limit the number of particles considered and it is shown that, above a threshold limit, the penetration curves become scale independent, provided a scalable crushing model is used. The particle crushing model parameters were calibrated by matching triaxial and one-dimensional compression tests. The DEM model could capture the stress measurements made around a model pile during and after its penetration into sand relatively well. The particle-scale mechanics that underlie the observed macroscopic responses are analysed, placing emphasis on the distribution of crushing events around the pile tip and distributions of particle stresses and forces around the shaft. Comparing simulations made with crushable and uncrushable grains, and analysing the particle displacement fields, provides insights into one of the mechanisms proposed for the well-known, yet not fully understood, marked shaft capacity increases developed over time by piles driven in sands.

RÉSUMÉ: Un modèle 3D d'éléments discrets (DEM) est utilisé pour prédire les expériences en chambre d'étalonnage de la pénétration de cônes et de pieux dans des supports pouvant être écrasés, à la fois par fonçage monotone et cyclique. Un modèle de broyage de particules basé sur un critère de rupture rigoureux pour les sphères élasto-fragiles est utilisé. Une mise à l'échelle des particules est réalisée pour limiter le nombre total de particules. Il est montré qu'au-delà d'un nombre minimum de particules, les courbes de pénétration deviennent indépendantes de leur taille, à condition qu'un modèle de broyage évolutif soit utilisé. Le modèle, calibré en faisant correspondre les tests de compression triaxiale et unidimensionnelle, fournit de bonnes prévisions pour les mesures de contrainte effectuées lors d'essais de pieux, pendant et après les phases de pénétration. Les caractéristiques micromécaniques expliquant les réponses macroscopiques observées sont analysées. Il s'agit notamment d'identifier la répartition de l'intensité de broyage autour de la pointe du pieu et d'analyser en détail les contraintes exercées par les particules et les chaînes de force autour du fût du pieu. La comparaison de simulations réalisées avec ou sans grains broyables, ainsi que l'analyse des champs de déplacement de particules, offrent une explication possible de l'impact bien connu, mais pas encore bien compris, du vieillissement sur la capacité du fût de pieux battus dans le sable.

Keywords: Discrete-element modelling, Piles, Particle crushing/crushability, Stress path, Stress analysis

1 INTRODUCTION

Improvements have been achieved in driven pile design through approaches such as those set out by Jardine et al., (2005) and Lehane et al., (2005). However, the full effective stress regime developed around piles driven in sands and the factors that control features such as their cyclic loading responses, group action and strong shaft capacity growth over time, remain incompletely fully understood; see Jardine (2013), (2019).

Calibration chamber experiments (Tehrani et al., 2018; Yang et al., 2014) and centrifuge tests (Bolton et al., 1999; Coop et al., 2005; Klotz and Coop, 2001) have highlighted the intense stress concentrations that develop below the pile tips, and also shown that pile geometry and driving cycles affect the final stress regime. Particle breakage, which is known to affect sands' mechanical behaviour significantly (Lade et al., 1996) also occurs during driving. Physical tests with highly instrumented piles and calibration chambers have identified aspects of the evolution of ground displacements and stresses around penetrating piles (Arshad et al., 2014; Doreau-Malioche et al., 2018; Jardine et al., 2013a; White and Bolton, 2004; White and Lehane, 2004). These programmes have provided benchmarks to test continuum modelling approaches for penetration problems (Gens et al., 2016; Monforte et al., 2017; Phuong et al., 2016) including treatments that consider particle breakage (Zhang et al., 2014, 2013).

The discrete element method (DEM), which considers individual soil particles and their interactions explicitly, can also be used to study large displacement contact problems and so provide fundamental insights into the mechanisms that underlie macroscopic behaviour (Santamarina, 2003). DEM has been applied to model monotonic 2D steady pile penetration (Huang and Ma, 1994; Jiang et al., 2014) as well as 3D cases (Arroyo et al., 2011; Butlanska et al., 2014; Butlanska and Arroyo, 2015; Janda and Ooi, 2016; Zhang and Wang, 2015). DEM analyses of dynamic penetration problems have also been reported (Tran et al., 2016; Zhang et al., 2018; Zhang and Evans, 2019) as have simulations of penetration in crushable media (Ciantia et al., 2016; Falagush et al., 2015; Zhang et al., 2018), pressurised grout injection (Boschi et al., 2019), and screw pile installation (Sharif et al., 2019).

This paper describes novel 3D DEM simulations that: a) are validated against experimental observations of the stress fields set up by pile penetration; b) test the hypothesis that arching forms around the pile shafts; c) examine the impact of cyclic jacking and particle crushing on the piles' micro-and macro mechanical behaviour. A computationally efficient DEM crushing model was employed to capture the load-deformation behaviour of the sand at high stresses, including grain crushing during one-dimensional compression (Ciantia et al., 2015) and shearing (Ciantia et al., 2019b). Parallel simulations involving crushable and unbreakable grains reveal how crushing accentuates stress relaxation close to the shaft and facilitates arching. Additional insights are given through analyses of the incremental radial displacements particles experience over each jacking cycle. The calibration chamber experiments reported by Rimoy et al. (2015), Jardine et al. (2013a), (2013b) and Yang et al. (2010), in which highly instrumented model piles were jacked into dense, pressurised, Fontainebleu NE34 sand, are adopted as a benchmark to test the simulations.

2 DEM PARTICLE CRUSHING MODEL AND NUMERICAL ANALYSES

2.1 DEM crushing model

The crushable DEM grain model of Ciantia et al. (2015, 2019b) was employed, which adopts a simplified Hertz-Mindlin contact law and spherical particles whose rotation is inhibited to capture the rotational resistances of angular grains (Arroyo et al. 2011; Calvetti 2008; Ting et al. 1989). The model's particle failure criterion follows Russell and Muir Wood (2009) and

Russell et al. (2009). Particles crush when any interparticle contact force reaches the limit:

$$F = \sigma_{lim} \cdot A_F \quad (1)$$

where σ_{lim} is the limit strength of the material and A_F is the contact area. Hertzian theory for smooth sphere contacts provides an expression for the contact area to give:

$$F \leq \left\{ \sigma_{lim} \pi \left[\frac{3}{4} \frac{\left(\frac{1-\nu_1^2}{E_1} + \frac{1-\nu_2^2}{E_2} \right)}{\left(\frac{1}{r_1} + \frac{1}{r_2} \right)} \right]^{\frac{2}{3}} \right\}^3 \quad (2)$$

where r_i (i=1,2) are the radii of the contacting spheres and E_i, ν_i are the Young's Moduli and Poisson's ratios respectively. To incorporate experimentally observed variability into the model, the limit strength, σ_{lim}, for a given sphere size is assumed to be normally distributed, which is incorporated through a correction factor, $f(var)$, that is applied to σ_{lim}. The coefficient of variation of the distribution, *var*, is considered to be a material parameter. A particle size dependency is also introduced to capture the relatively higher strength of smaller particles; this takes a Weibull-like form, where the limit strength is given by:

$$\sigma_{lim} = \sigma_{lim} f(var) \left(\frac{d}{N d_0} \right)^{\frac{-3}{m}} \quad (3)$$

where m is a material constant, σ_{lim0} is the mean limit strength at the reference diameter, d_0, (taken to be 2 mm here) and N is the scaling factor. The failure criterion remains unchanged for particle-wall contacts; the wall is considered as particle 2 so that the elastic properties of the wall are used to select E_2 and ν_2 and the ratio $1/r_2$ is taken as 0 as the wall radius far exceeds that of the particles.

Once the crushing limit condition is reached, the spherical particles are split into smaller inscribed tangent spheres, corresponding to the first steps of an Apollonian series. The spawned fragments assume the velocity and material parameters of the original particle apart from the intrinsic strength (σ_{lim}) which is reassigned using eq. (3).To track the evolution of the PSD, the breakage index *Br* (Einav, 2007), is computed continuously. The limit grading is given by a fractal distribution with fractal dimension ω=2.6, which (Einav, 2007) expressed as:

$$\frac{M_{(L<d)}}{M_T} = \frac{d^{3-\omega} - d_{min}^{3-\omega}}{d_{max}^{3-\omega} - d_{min}^{3-\omega}} \quad (4)$$

where M_T is the total mass, $M_{(L<d)}$ the mass of particles smaller than d, d_{max} and d_{min} are, respectively, the maximum and minimum particle sizes assumed for the limit distribution. Following Ciantia et al. (2015) a numerically motivated comminution limit, d_{comm}, is imposed to halt the production of excessively small particles. The crushing model was implemented in PFC3D-V5 (Itasca, 2016).

Table 1. Calibrated model parameters for FS grains

d_{50}	μ	G	ν	$\sigma_{lim,0}$	m
mm	-	GPa	-	GPa	-
0.21	0.275	9	0.2	1.9	10
d_0	*var*	d_{comm}/d_{50}	d_{max}	d_{min}	D_{loc}
mm	-	-	mm	mm	-
2	0.36	0.55	0.27	0.01	0.05

The model parameters used in the current study, listed on Table 1 are those obtained in an extensive calibration exercise that considered Fontainebleau sand, Figure 1 (Ciantia et al., 2019b). Comparisons are given in (a) of the experimental and numerical particle size distributions. Simulations and outcomes from triaxial tests performed from p' = 100 kPa are compared in (b), while parallel oedometer test conditions are presented in (c) and the corresponding evolutions of particle size distributions are shown in (d). In line with the proposal made by Muir Wood (2007) and Muir Wood & Maeda (2008), Altuhafi et al., (2018b) show that Fontainebleu sand develops an infinite possible family of critical state lines as its particle distribution profile evolves under high pressure shearing that together constitute a

unique critical state plane (CSP). Ciantia et al., (2019b) show that the adopted DEM model can reproduce the experimental trends found by Altuhafi et al. (2018a). The ability to capture the behaviour of highly overconsolidated, pre-crushed, sand is important to the pile simulations as particles near the axis experience extreme loading as the tip penetrates into any given layer within the sand mass, and then undergo very significant unloading as the pile tip advances to greater depth

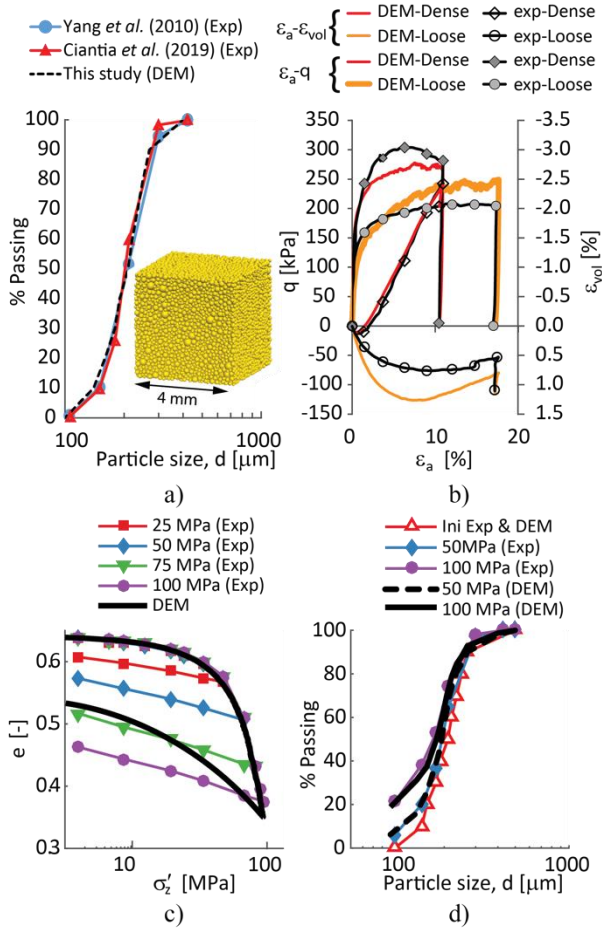

Figure 1 Contact model calibration from Ciantia et al. (2019a): a) Experimental and numerical PSD and DEM model at 5kPa isotropic compression pressure, b) DEM simulation of drained triaxial compression test (cell pressure 100 kPa; experimental data from Seif El Dine et al., 2010). Crushing model validation by DEM simulation of high-pressure oedometer tests in terms of c) effective vertical stress vs void ratio and d) PSD evolution.

3 ANALYSIS OF CONE-ENDED PENETRATION TEST IN FONTAINEBLEAU SAND

The calibrated DEM crushing model was adopted to simulate the cone-ended model pile tests described by Yang et al. (2010). An important feature to emerge from the physical experiments was the considerable difference between the sand stresses developed during steady penetration (the push phases of jacking cycles) and those that applied when the pile was stationary without any pile head load during the jacking-cycle pause phases; see (Jardine et al., 2013b). The DEM analyses considered both cases. Where possible, the results of the FEM steady penetration conditions simulated by Zhang et al. (2013) are compared with the DEM predictions.

3.1 DEM Model Construction

A DEM 'model calibration chamber' was developed to match the physical experiments by Yang et al. (2010) as closely as was feasible, as summarised in Table 2 and illustrated in Figure 2(a). Noting that Coetzee (2019) showed that particle scaling is a viable approach when using DEM to model large scale boundary value problems, the particles were scaled up by a factor of 39, while adhering to the Fontainebleau sand's particle size distribution curve's normalised shape. This allowed the analyses to proceed with four orders of magnitude fewer particles than in the experiments and led to a computationally feasible 442,335 particles. Falagush et al. (2015) showed that when using a non-scalable crushing law and adjusting particle sizes leads to unphysical results because of particle strength size effects. In the present analyses the crushing law used is scalable and so avoids the unrealistic results possible when scaling is not considered.

The calibration chamber (CC) instrumented pile tests were performed under a no-strain, low friction, radial lateral condition. The experimental chamber's vertical boundaries were located 33.7*R*, where *R* is the pile radius, *R* from

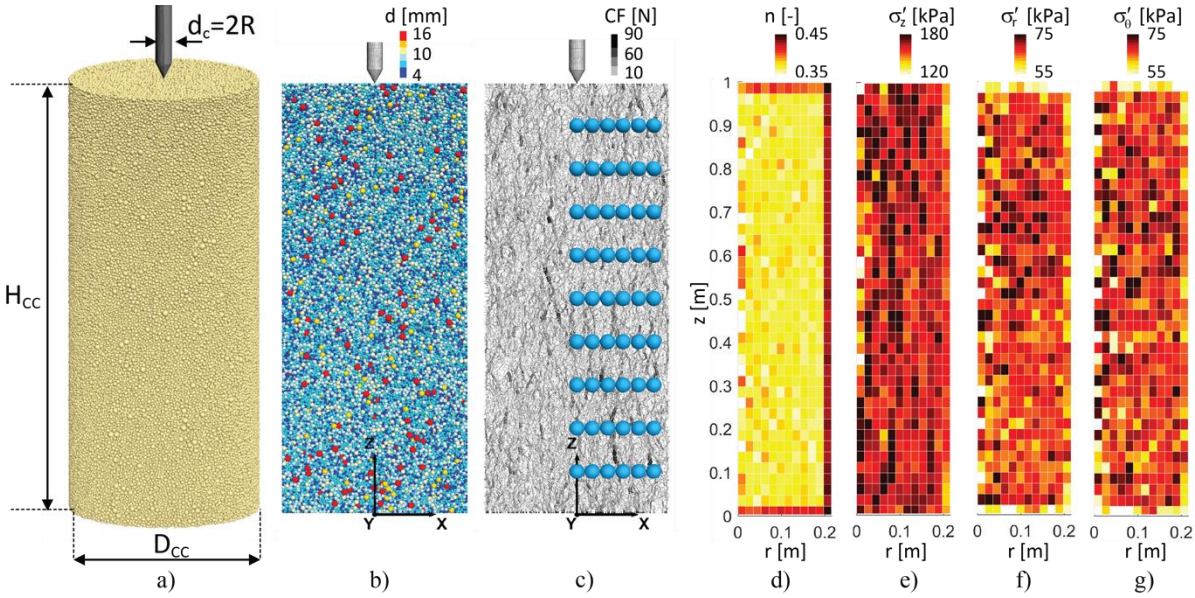

Figure 2 Initial condition of DEM model: a) 3D view, b) 2D cross section showing particle diameter, c) contact forces and position of measurement spheres (MSs), initial porosity (d), vertical stress (e) radial stress (f) and circumferential stress (g) contours.

the pile axis; still larger ratios are required to simulate field behaviour accurately (Pournaghiazar et al., 2013; Salgado et al., 1998). To make the DEM modelling feasible, frictionless radial walls preventing circumferential motion of particles were placed at a smaller radial distance 12*R* from the centre of the pile noting that the experimentally measured radial, vertical and tangential stresses during penetration were relatively stable at this distance from the pile axis (Jardine et al., 2013a). Adopting a larger radial distance for the modelling would have been more representative. However, capturing even the test chamber dimensions would have required approximately 3 million extra (scaled-up) particles and rendered the analyses impossible to achieve with the adopted software and available computers.

Techniques employed to decrease boundary effects in DEM models include the particle refinement method, using larger radial walls (McDowell et al., 2012) and coupled DEM-FEM approaches (Tu et al., 2017). The former was not used, as the model was designed to have the same level of resolution across the whole chamber. Unfortunately, coupled software was not available to follow the second route. Instead, the particle-lateral chamber wall contacts where assigned a stiffness equal to the particle stiffness to mimic the far-field response. The match shown later between the DEM and the experimental penetration resistance and stress profiles indicate that this step led to reasonable overall outcomes, although other approaches could also have been followed.

Table 2. Comparative geometrical characteristics of experimental and simulated (DEM) calibration chamber.

Variable (unit)	**Symbol**	**Experiments**	**DEM Model**
Chamber diameter (mm)	D_{CC}	1200	432
Cone diameter (mm)	d_c	36	36
Chamber height (mm)	H_{CC}	1500	1000
Particle median size (mm)	d_{50}	0.21	8.19
Initial number of particles	N_p	$3x10^{11}$*	442335
Chamber/cone ratio D_C/d_c	R_d	33.7	12
Cone /particle ratio d_c/d_{50}	n_p	171.4	4.4
Stress cell diameter/particle ratio d_{cell}/d_{50}	n_s	28-31	4.4
Number of stress cells	N_{cells}	36	54
Average porosity	n	0.382	0.38
Average CC σ_z' (kPa)	$\bar{\sigma}_z'$	150	152.9
Initial CC σ_r' (kPa)	$\bar{\sigma}_r'$	76	76.7

*approximate

The experiments employed sand air-pluviated to an initial porosity n=0.382, and relative density Dr=72%. Simulating such a procedure in DEM is computationally very demanding (Ciantia et al., 2017), so the 'DEM chamber' was filled with scaled-up grains using the radius expansion method (Itasca, 2016) as described by Ciantia et al. (2018). In the experiments a constant 150 kPa vertical stress was maintained along the top boundary and there was a rigid wall at the base. In the DEM model, the top (frictionless) horizontal boundary was servo-controlled to apply the desired vertical stress level while both the bottom (frictionless) wall was fixed. To match the initial stress conditions in the experiments, the DEM specimen was first formed at a target initial porosity of 0.385 at 5 kPa of isotropic pressure followed by an axial compression to the 150 kPa target vertical stress. The exterior horizontal stress was adjusted to match the experimental 76 kPa value by using radial wall servo-control, giving a mean effective stress p'=101 kPa and a final average porosity of 0.383 (Figure 2(d)).

The pile shaft and tip were modelled using rigid frictional cylindrical walls with the interface friction coefficient set equal to the critical state value ($\tan\delta$ =0.5) measured in interface ring-shear tests conducted against surfaces composed of the same stainless steel as the pile and with the same surface roughness (Yang et al., 2010). The particle-pile contacts employed a simplified Hertz-Mindlin contact model with the pile shear modulus (G_{pile}) and Poisson's ratio (ν_{pile}) set to 85 GPa and 0.2 respectively (Young Modulus of 200 GPa); the pile was therefore effectively rigid relative to the particulate assembly. The pile-to-median particle diameter ratio, n_p, was 4.4 in the DEM model which this is much smaller than the experimental value of 36 but larger than other published 3D DEM penetration simulations (Table 3). The low n_p ratio increased the scatter (or fluctuations) in the stress predictions made for the penetrating pile (Arroyo et al. (2011); Butlanska et al. (2014)).

Such scatter can only be avoided by employing smaller particles, which then render the analysis computationally unfeasible. However, the fluctuations can be filtered out by fitting appropriate penetration trend lines through the scatter. The exponential expression applied in Arroyo et al., (2011) was used in the present analyses to establish smooth pile end-bearing pressure versus tip-depth trend $q_{c,trend}$ where:

$$q_{c,trend}(h_p) = a[1 - exp(-bh_p)] \quad (5)$$

where h_p is the penetration depth and a and b are fitting parameters. The parameter a gives the asymptotic or steady state value of cone resistance. The influence of the cone penetration velocity was investigated to ensure quasi-static conditions were achieved during penetration. The inertial

Table 3. 3D DEM numerical penetration model characteristics

Symbol	**This study**	(Arroyo et al., 2011)	(Ciantia et al., 2016)	(Janda and Ooi, 2016)	(Zhang and Wang, 2015)	(Zhang and Evans, 2019)	(Zhang et al., 2019)
D_C (mm)	432	1200	760	101	12	20000	760
d_c (mm)	36	71.2	36	12.83	1	2100	50.8
H_{cc} (mm)	1000	700	760	250	24	25000	500
d_{50} (mm)	8.19	26.5	15	5	0.172	500	16.6
N (-)	39	50	15	-	1	-	79
N_p (-)	442,335	65,000	203,000	15,000	608,088	-	60,000
Rd (-)	12	16.9	21	7.87	12	11.9	15
n_p (-)	4.4	2.7	2.4	2.57	5.8	4.2	3.06
n_s (-)	4.4	1.89*	-	-	2.9	-	-
N_{cells} (-)	54	45*	-	-	2	-	-

*Reported in Butlanska et al. (2009)

number, *I*, can be used to characterize dynamic effects in systems under shear:

$$I = \dot{\gamma} d_{50} \sqrt{\rho / P} \tag{6}$$

Where $\dot{\gamma}$ is the shear strain rate, d_{50} is the median diameter of the particles, ρ is the particle density and P is the confining pressure. In their penetration simulations Janda and Ooi (2016) assumed $I<10^{-2}$ for quasi-static conditions; giving $\dot{\gamma}<7.6s^{-1}$ when P is taken as the initial p' (101 kPa), ρ as the particle density (2600 kg/m^3) and d_{med} as 8.9mm. The cone penetration velocity was then calculated as:

$$v_{pile} = \dot{\gamma} L_p \tag{7}$$

where L_p is the width of the plastic zone formed under the tip which, following Lu et al. (2004), was assumed to be $3d_c$. Assuming $\dot{\gamma}=7.6s^{-1}$ gives v_{pile}= 0.8 m/s. Since Butlanska et al. (2010) showed that for similar particle masses rates between 0.02 and 0.50 m/s do not change the simulation results, an optimum value of 0.50 m/s was adopted. This is below the 1 m/s limit where dynamic effects have been documented as appearing by Janda and Ooi (2016), Quezada et al. (2014) and Tran et al. (2016b).

To simulate cyclic pile jacking, after each 100 mm of penetration, the pile was unloaded by slowly displacing it upwards until the vertical head force was zero. These jack strokes were repeated until 1m penetration was achieved. Two monotonic simulations (where no unloading was simulated) were also performed, one of which was run without invoking particle breakage.

As illustrated in Figure 2(c), thirty six measurement spheres (MS) each with a diameter equal to the cone diameter, were placed in the DEM model domain to allow frequent measurement of the average soil stresses. In each sphere the stress is computed as (Christoffersen et al., 1981):

$$\boldsymbol{\sigma}' = \frac{1}{V_{MS}} \sum_{N^c} \boldsymbol{F}^c \otimes \boldsymbol{L}^c \tag{8}$$

where N^c is the number of contacts that lie in the measurement region of volume V_{MS}, $\boldsymbol{F}^c$ is the contact force vector, $\boldsymbol{L}^c$ is the branch vector joining the centroids of the two bodies in contact, $\otimes$ denotes the outer (tensor) product.

The particle and contact model data were saved and processed externally at the end of each push and pause (unload) period, enabling the stresses to be calculated within any portion of the model domain. To do so, the particle Cartesian stress tensor ($\bar{\boldsymbol{\sigma}}^p$) was calculated following Luding, (2004):

$$\bar{\boldsymbol{\sigma}}^p = \frac{1}{V_p} \sum_{c=1}^{Nc,p} \boldsymbol{s}^c \otimes \boldsymbol{F}^c \tag{9}$$

where the superscripts indicate particle (p) or contact (c). $N^{c,p}$ is the number of contacts involving particle p, $\boldsymbol{s}^c$ is the vector connecting the element centre with the contact point and $\boldsymbol{F}^c$ is the contact force vector. These data can be used to compute the average stress for a volume V containing of N^p particles (each having volume V^p) as follows:

$$\boldsymbol{\sigma}' = \frac{1}{V} \sum_{N^p} \bar{\boldsymbol{\sigma}}^p V^p \tag{10}$$

The mean effective stress p' and the deviatoric stress q are given by

$$p' = \frac{1}{3} tr(\boldsymbol{\sigma}') \tag{11}$$

$$q = \sqrt{\frac{2}{3}} \|\boldsymbol{s}\| \tag{12}$$

where $\boldsymbol{s} = \boldsymbol{\sigma} - p\boldsymbol{I}$, $\|\boldsymbol{s}\|$ denotes the Euclidian norm of $\boldsymbol{s}$ and $\boldsymbol{I}$ is the second order identity tensor. Assuming axisymmetric conditions, the stress state of the soil can be described using the radial stress σ_r', the circumferential stress σ_θ', the vertical stress σ_z' and the shear stress τ_{zr}'.

The homogeneities of initial sand chamber porosities and stresses were considered before commencing pile penetration by considering 480 annular rings each having a width equal to the pile radius and a height of 25 mm. The ring size was chosen to give an optimal balance between resolution, which decreases with increasing ring size, and achieving a statistically representative volume which requires a minimum number of particles. The minimum number of particles in any averaging ring was 65. Stresses were calculated using equation (10) taking care that only the portions of the particle volumes (V^p) inside each averaging volume V were considered. Sections were taken through these rings and the average stress or porosity in each ring was displayed according to a colour scale. As expected and represented in Figure 2(d) higher porosity values are measured near to the rigid walls (Huang et al., 2014) while the internal mass is more homogeneous. As shown in Figure 2(e-g) the DEM sample also experienced relatively homogenous initial stresses: the mean vertical, radial, and circumferential stresses are 152.9 kPa, 76.7 kPa and 76.8 kPa with a standard deviation of 12 kPa, 4.9 kPa and 5.1 kPa respectively. Table 2 compares these averages with the experimental target values.

3.2 *Macroscale results*

Figure 3(a) gives the penetration data from both the monotonic and the cyclically jacked DEM simulations and their corresponding fitted penetration curves. The cyclic and monotonic DEM numerical simulations give very similar curves, suggesting that the cycling process has little influence on the end bearing capacity q_c, as found in the calibration chamber experiments by Yang et al. (2010). However, when crushing is disabled the cone resistance rises 50% above the crushable model response (around 20 MPa). These results are combined with those from other DEM and experimental studies and plotted as q_c (uncrushable particles)/q_c(crushable) versus initial relative density in Figure 3(b). The analyses described herein conform with the trends from the earlier experimental studies and DEM simulations cited above.

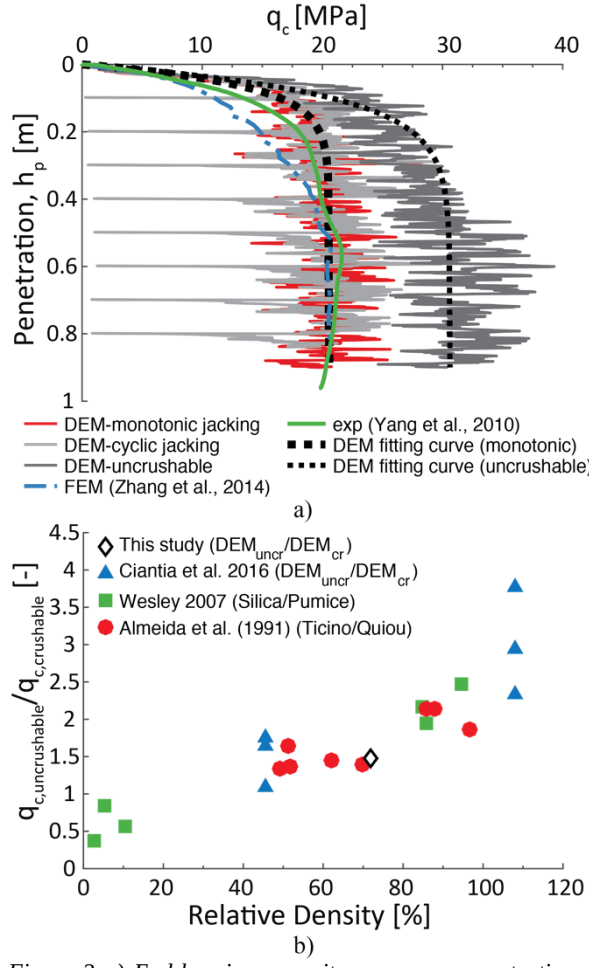

Figure 3 a) End-bearing capacity q_c versus penetration: Comparison between DEM (raw data and fitting curve), FEM (Zhang et al., 2014) (steady state q_c = 21 MPa)and experimental results (Yang et al., 2010) and b) effect of crushability on tip resistance (Ciantia et al., 2016).

3.3 *Stress distributions: comparison of DEM model predictions with experiments and FE simulations*

Figure 4 compares the experimental and DEM outcomes for σ'_r considering stress measurements at r=2R (R=pile radius) and three depths below the sand surface during the push phase of the jacking cycle. There is generally good agreement

between the experimental stresses the model predictions. However, the agreement becomes less satisfactory once the tip has penetrated 50 mm below the measurement point. Given that the displacement fields are largely controlled by the pile tip geometry, the stress discrepancy may be due to the contact model predicting that the DEM model's unloading response is softer (see Figure 1c) than is seen experimentally.

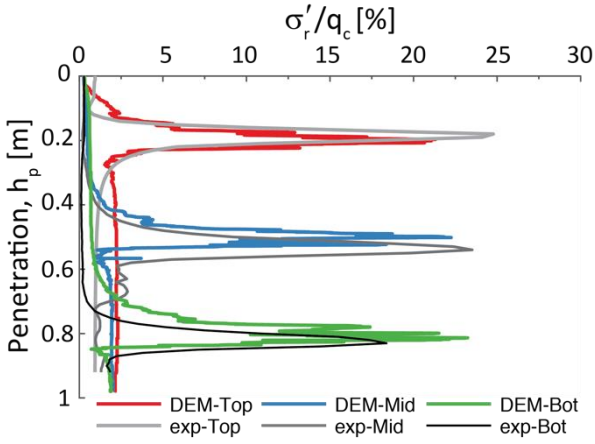

Figure 4 DEM and experimental (Jardine et al., 2013a) normalised radial stresses measured at r =2R for three different locations in the soil (20cm, 50cm and 80cm from the top boundary) as the pile is installed.

The radial stress regime developed in the sand beneath and above the moving pile tip is further explored in Figure 5. To be consistent with (Jardine et al., 2013a) the data are represented as a function of relative pile tip depth *h* normalized by pile radius *R*. Note that *h/R* is initially negative, and becomes positive when the penetrating tip reaches each stress measurement particular level. Data are plotted for Three *r/R* positions and the circumferential (σ'_θ) and vertical (σ'_z) stresses are also reported. Over the *r/R* ranges considered, the DEM predictions are in good agreement with the experimental profile shapes, their positions and peak magnitudes.

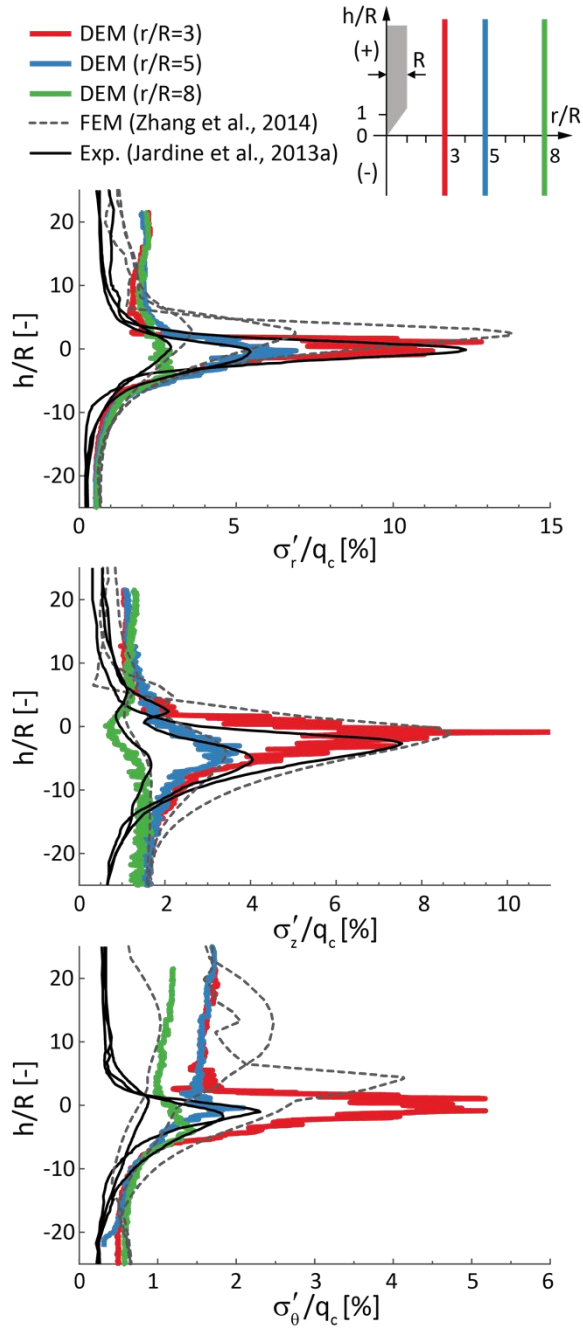

Figure 5 DEM, FEM (Zhang et al., 2014) and experimental (Jardine et al., 2013a) comparison of stresses developed as pile tip advances. The radial (b) circumferential (c) and vertical (d) stresses are normalized by q_c and refer to lines having at a distance r/R=3,5 and 8 from the pile axis as sketched in (a).

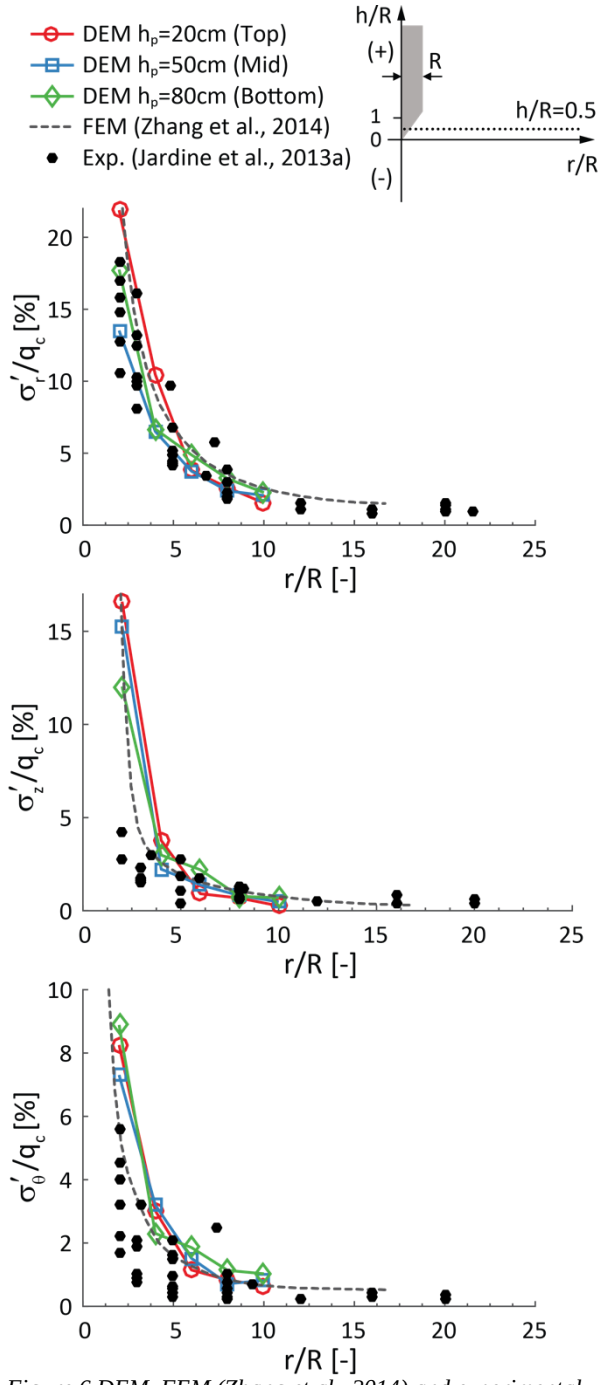

Figure 6 DEM, FEM (Zhang et al., 2014) and experimental (Jardine et al., 2013a) comparison of normalized radial (b) tangential (c) and vertical (d) effective stress evolutions along the radial axis at h=0.5R above the tip.

Figure 6 considers the decay of the σ'_r, σ'_θ and σ'_z stresses (normalized by q_c) with increasing *r/R* during the penetrating phases of the jacking cycles. These values are established at *h/R=0.5* at three penetration stages (all three in the steady state regime) and compared with the Jardine et al. (2013a) experimental data. The same experiments were simulated using the finite element method (FEM) by Zhang et al. (2014). It is interesting that the FEM and DEM analyses both show similar exponential decays to the experiments, even close to the tip where numerical analyses predictions are most difficult to predict accurately (Gupta,1991).

As with the numerical simulation data, Jardine et al. (2013a) report that measurements made close to the pile tip are subject to relatively high coefficients of variation (COVs). While the DEM σ'_r trend follows the experimental data at all plotted *r/R* ratios, the σ'_θ/q_c and σ'_z/q_c predictions tend to exceed the experimental trends, especially close to the pile shaft (*r/R*<3).

Figure 7 summarises the spatial variation of radial effective stress normalized by q_c at three stages of penetration, considering both loaded push period (push) and zero-load pause period (pause) phases of the cyclic jacking process. In line with the results presented in Figure 5, the stress distributions below and around the tip appear to depend principally on *h/R* and *r/R* and to be independent of the absolute penetration depths for the conditions considered. However, the stresses applying around the shaft are influenced by the top boundary condition over the first 200-300 mm below the sand surface, after which the end-bearing penetration curve achieves its quasi-steady state regime (see Figure 3). This is more evident in the 'pause' contours (Figure 7b) where a peak of radial stresses develops at about 50-60 mm out from the axis (at *r/R*≈3) along the shaft length below the region that is influenced by the top boundary (0.0< *z* <0.2).

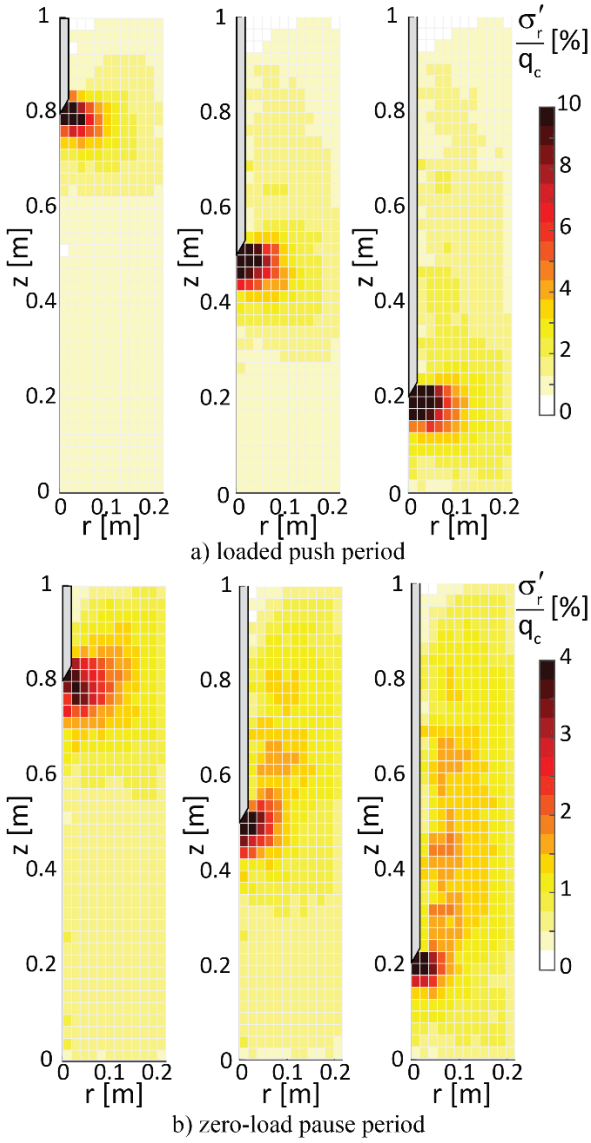

Figure 7 Illustration of radial stress spatial distribution, normalised by q_c, shown in %, during installation for three penetration depths: (a) 'penetrating' conditions at end of push; (b) 'unloaded' at end of each corresponding pause.

To better investigate the stress evolution around the pile tip, the spatial variations of σ'_r, σ'_θ and σ'_z around the shaft are presented in Figures 8 and 9 (normalised by q_c) for the penetrating and (unloaded) pause conditions. The numerical predictions are in broadly good agreement with the experimental contour plots given by Jardine et al. (2013b).

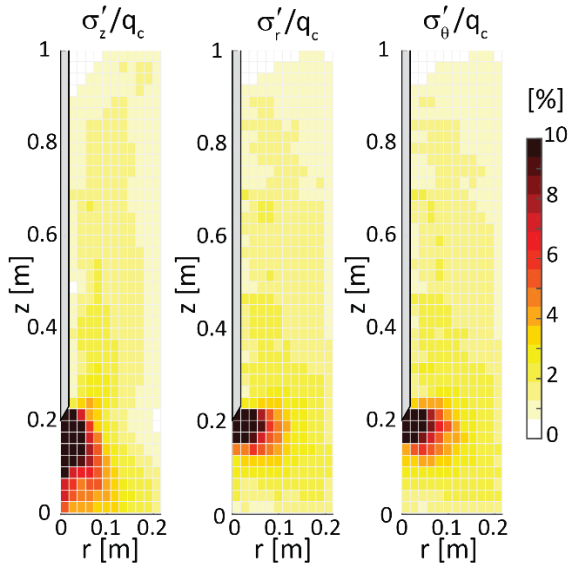

Figure 8 Illustration of DEM stress spatial distribution of stresses normalised by q_c during the loaded push period. Experimental contours are reported in Jardine et al. (2013b).

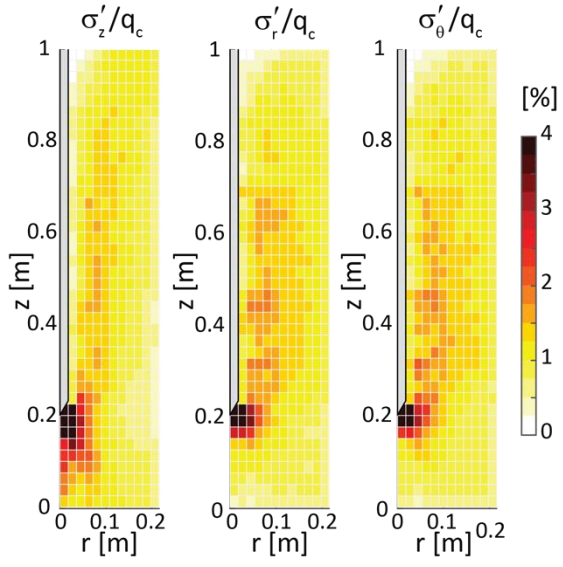

Figure 9 Illustration of DEM stress spatial distribution of stresses normalised by q_c during zero-load pause period. Experimental contours are reported in Jardine et al. (2013b).

This is confirmed in Figure 10 where radial profiles of the stresses are represented for three positions above the shaft and compared when possible with experimental data (from Jardine et al. (2013b)) and FEM predictions by Zhang et al.

(2014), who did not consider the pause stages explicitly. The FEM and (smoothed) DEM analyses led to similar peak stress ratios and generally comparable trends. The DEM predictions for the pause periods also show fair agreement with the experimental data, particularly for the radial stress cases for which there were more sensors and lower potential measurement errors and scatter; Jardine et al (2013a).

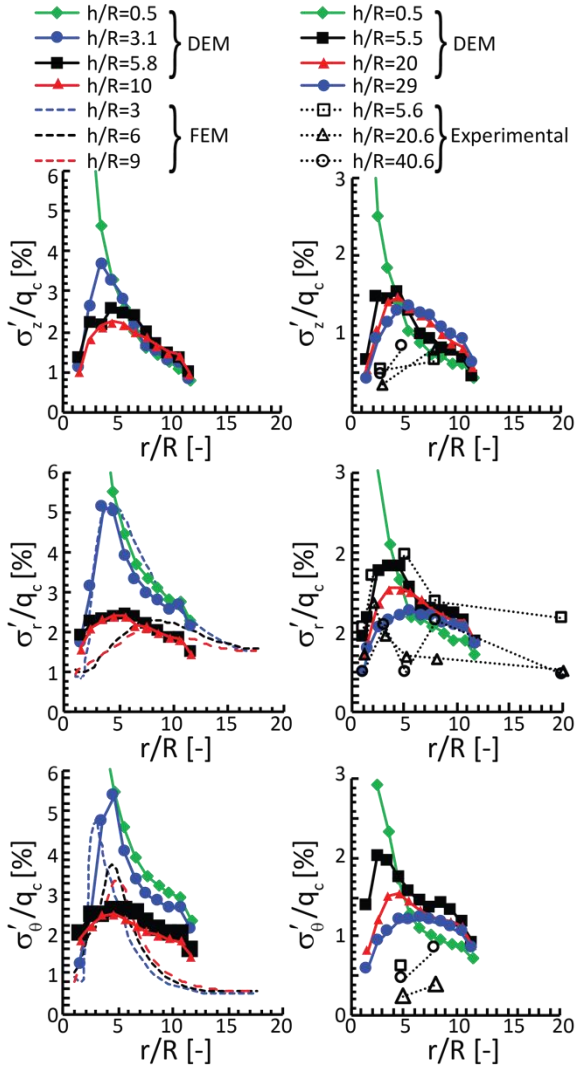

Figure 10 DEM vertical radial and circumferential stresses acting above pile tip during: (a) steady penetration and (b) (unloaded) pause conditions. Where possible FEM and experimental results are also shown.

Further insight into the extreme stress changes that apply around pile shafts during penetration into sand is given by considering the stresses experienced at the h/R=0.5 stage (Figure 10). The soil around the shaft (r/R<5) unloads very significantly as the pile tip passes, while further way (at r/R>5) the stress relaxation is relatively modest. These opposing trends leads to the stress profiles presenting their maxima at 3R-5R from the pile axis.

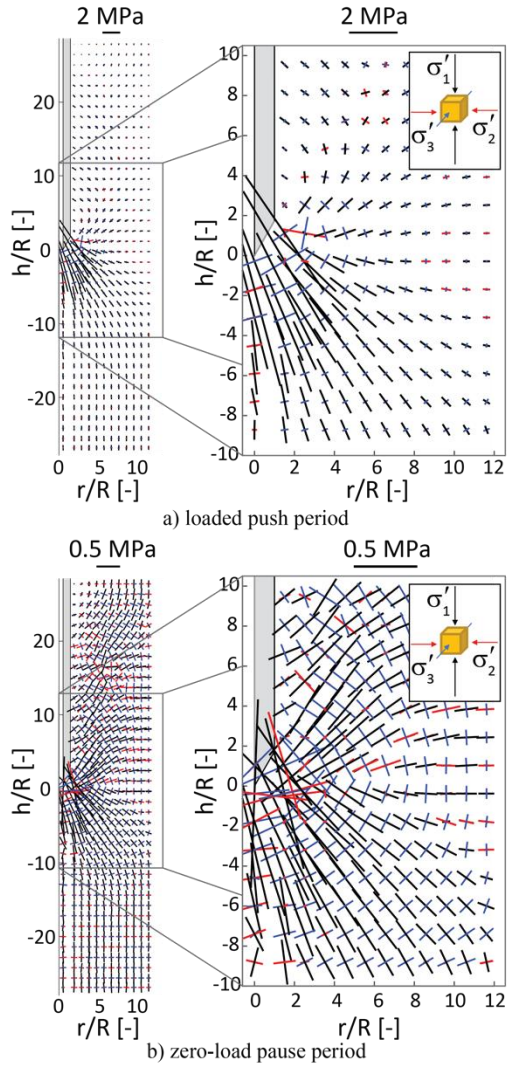

Figure 11 Major (σ_1' in black), intermediate (σ_2' in red) and minor (σ_3' in blue) principal stress vectors for (a) 'penetrating' conditions at end of the h_p=0.5 push phase; (b) 'unloaded' at end of the corresponding pause period.

The stress analyses presented above considered only the σ'_r, σ'_θ and σ'_z cylindrical components. While the initial stress regime has $\sigma'_z=\sigma'_1$ and $\sigma'_r=\sigma'_\theta=\sigma'_2=\sigma'_3$ as its principal stresses Figure 11a demonstrates the intensive rotation (up to 250º) of the major principal stress axes that take place in the sand mass as the pile penetrates. Jiang et al. (2006) report similar overall trends from their 2D DEM simulations.

As depicted in Figure 11(b), the unloading associated with the jacking pauses induces further rotations of the principal stress axes close to the shaft. Interestingly, the spatial distribution of the major principal stress axis directions resemble closely the principal strain increment axis directions interpreted by Galvis-Castro et al. (2019) from model pile calibration chamber experiments through digital image correlation. While closer correlation checks are required between the principal stress and strain axes' directions, it appears that pile penetration in sands provokes a largely co-axial mechanical behavioural response.

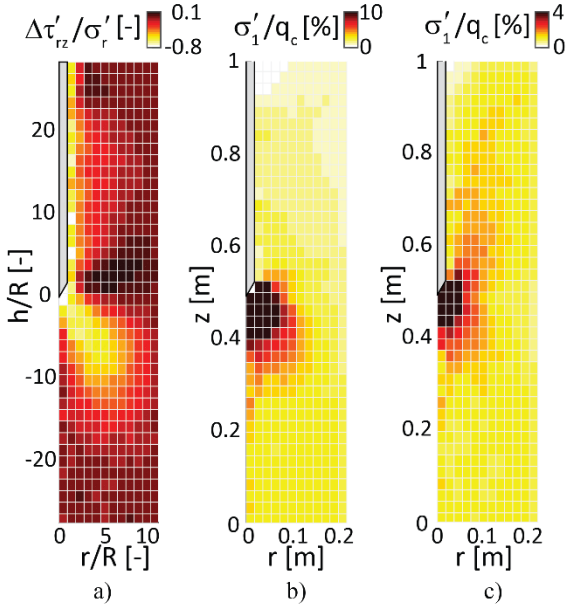

Figure 12 spatial distributions of a) changes of normalized vertical shear stress between 'push' and 'pause' stages. Parts b) and c) present magnitudes of major principal stress (σ'_1) normalized by q_c covering the penetration and (unloaded) conditions respectively.

The spatial variations in σ'_1 shown in Figure 12b) and c) confirm that the major principal stress significantly reduces around the pile tip shoulder as *h/R* grows. The marked stress axis rotation is induced by the change in direction of the vertical shaft shear stresses, which are represented in Figure 12(c) normalised by the radial (effective) stress.

3.4 Microscale insights: particle breakage and arching

Comparisons between DEM simulations performed with and without particle breakage allow evaluation of the separate impacts on the stress relaxation experienced around the shaft of grain crushing. Considering a measurement sphere whose origin is positioned at *r/R*=2 and *z*=0.5m, at the chamber mid-height. Figure 13 tracks how the mobilised stress ratio *q/p´* varies with *h/R*.

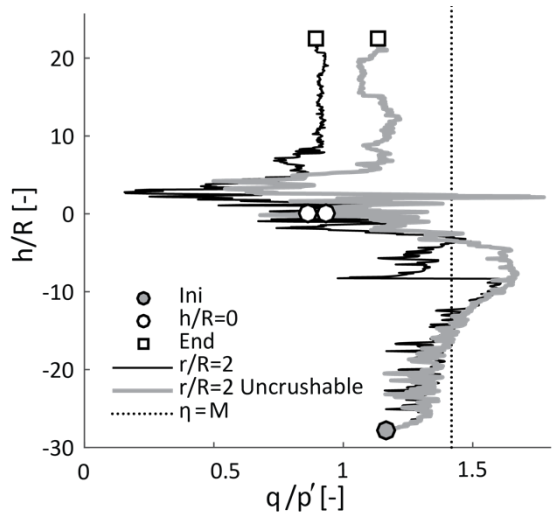

Figure 13 Evolution of stress ratio (q/p') measured during pile monotonic penetration at r=2R form pile axis for MS at z=0.5 for the crushable (black) and uncrushable (grey) case.

With crushable grains, the *q/p'* ratio reaches its peak at *h/R*= -8 after which it falls, passing through critical state at *h/R*=-1 and then starts to decrease, indicating shear unloading. The uncrushable grain analysis does not show the

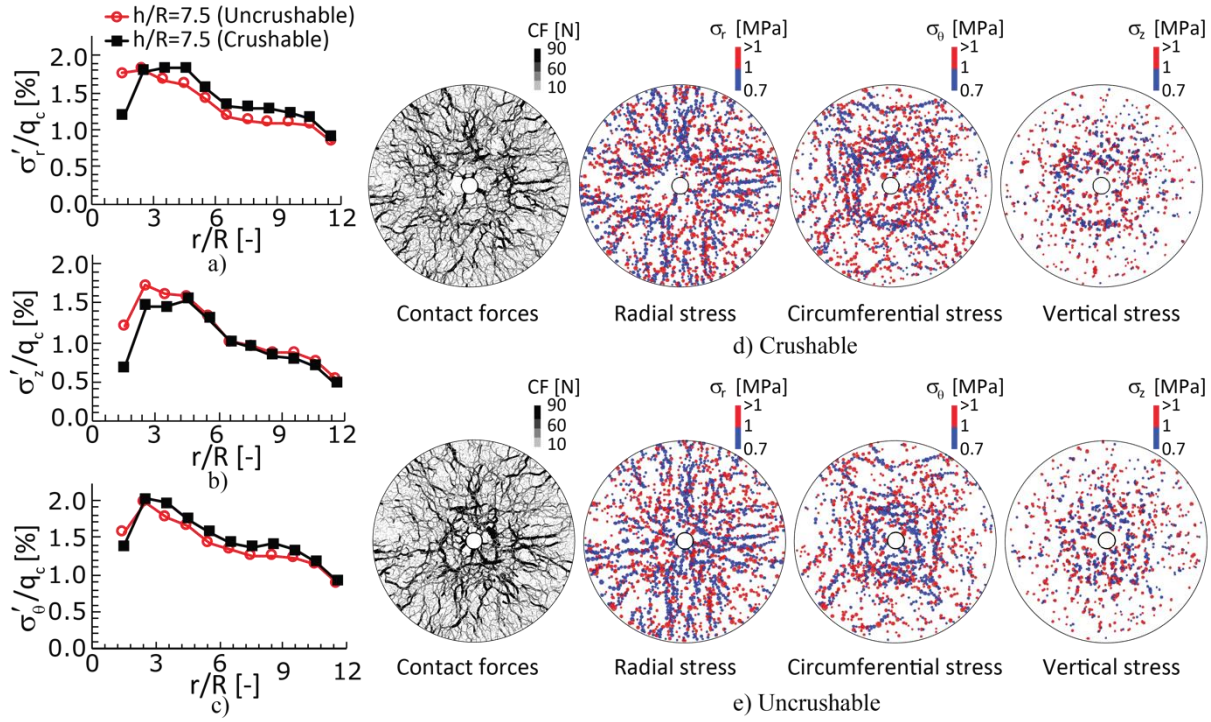

Figure 14 Radial profiles of (a) radial, (b) circumferential and (c) vertical stresses acting at h/R=7.5, comparing crushable and uncrushable simulations of the (unloaded) pause phases and demonstrating arching around the pile shaft: d) Uncrushable e) Crushable. Only particles with circumferential, radial and vertical stress>0.7MPa are shown: blue > 1MPa and red<1MPa

same sharp drop in q/p' when h/R passes the maximum (peak q/p' value). Nevertheless, q, p' and q/p' decrease as the pile tip penetrates to give h/R >0.6 in both cases and shear unloading reaches a minimum once h/R reaches ≈3.

The stress ratio subsequently increases slightly until a stationary value is obtained. However, the crushable grain case involves a greater degree of shear unloading further from the tip (at h/R>5) than is predicted to apply to unbreakable grains.

Parts (a), (b) and (c) of Figure 14 compare the radial profiles of the cylindrical stress components (normalised by q_c of the crushable response) given from analyses with crushable and unbreakable grains at h/R=7.5 above the tip, considering a zero-load pause period jacking stage of a cycle. Crushing accentuates the unloading close to the shaft and promotes the arching action.

It is possible to construct images of the associated contact force network by representing each contact force as a line (with thickness proportional to its force) that joins the centres of contacting particles. Vertical plan views of the force networks predicted around the shaft at h/R=7.5 for the uncrushable and crushable cases are shown in Figures 14(d) and (e), which are broken down into radial, circumferential and vertical sets to highlight how crushing affects the force chain systems. Circumferentially arching force networks are more clearly developed around the shaft in the crushable case that shield the pile shaft surface (at r/R=1) from the higher radial stresses developed at greater r/R and lead to more weekly developed radial force networks close to the shaft.

Figure 15 provides further insights into the arch development by showing the incremental particle displacements developed during the penetration and (unloaded) pause phases of the jacking cycle that advanced the pile tip from 0.7 to

0.8 m depth. Particles located below the tip experience large radial displacements away from the axis tip, while those just above the tip move radially inwards (by far smaller degrees) and promote radial stress relaxation (see Figure 11a) in both the crushable and uncrushable simulations although more inward radial displacement applies in the uncrushable case during the zero-load pause period.

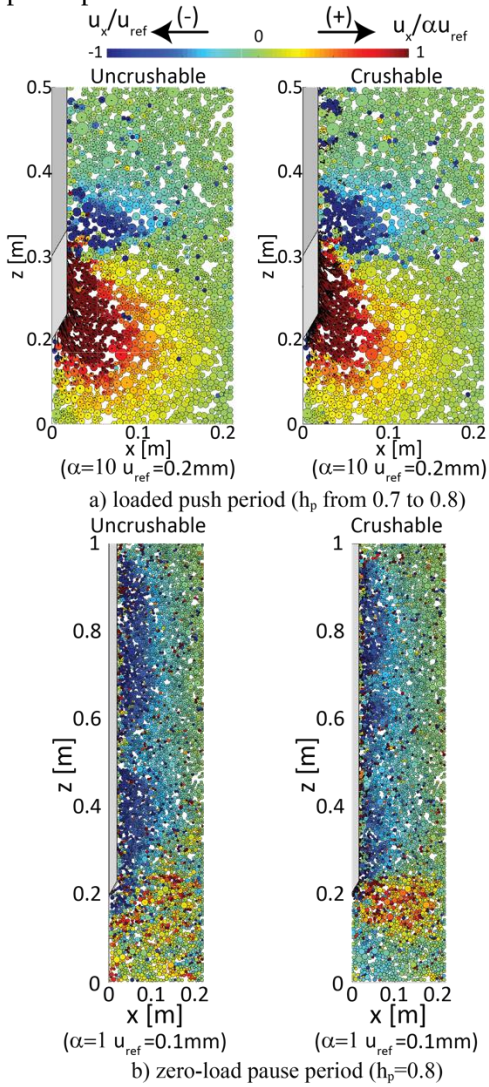

Figure 15 Comparison of particle radial displacement increments for the crushable and uncrushable models during a) 10cm of penetration (0.7 to 0.8m of penetration dept h_p) and b) the following zero-load pause period: the negative values (towards the shaft) are normalised by u_{ref}, the positive values (away from the pile) are normalised by αu_{ref}.

Jardine et al (2006) and Jardine (2019) argue that the non-uniform stress distributions set up by driven pile installation provide one of the potential mechanisms for the marked growth of shaft capacity over time developed by piles driven in sand. Creep could weaken circumferential arching and lead to radial stresses (and shaft resistances) rising. Corrosion reactions and other processes can also be important, particularly with small diameter piles: see Carroll et al (2019).

Particle breakage clearly affects the particle movements and stress redistributions around the pile shafts. Recent acoustic emission (AE) and signal processing (Mao et al., 2018, 2016) studies have revealed that, for flat ended piles, particle breakage develops principally under the pile tip within an area located between 0.5-1.5 pile diameters below the tip. Doreau-Malioche et al. (2018) by means of X-Ray imaging show that it is possible to identify the location of crushed fragments around a small-scale displacement pile penetrating through a crushable carbonate sand and show that crushing develops principally around the tip.

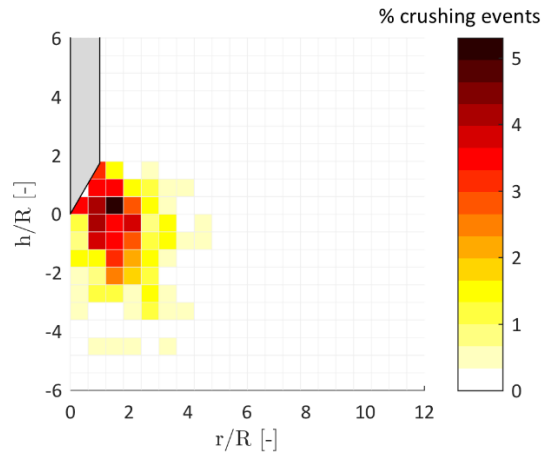

Figure 16 Particle crushing location during pile penetration represented as % of crushing events with respect to tip position.

Figure 16 provides a representation in *h/R*, *r/R* coordinates of the positions at which all particle breakage is predicted in the DEM analyses of pile penetration. The DEM model predicts that most

crushing occurs close to the cone, within a volume described by a triangular, convex shaped, solid of revolution with characteristic length of about 1.5*R*. In line with the experimental evidence mentioned above, no crushing events are predicted at distances 5*R* below the tip or above the pile tip shoulder. The crushed fragments are first pushed away from the axis and then move back towards the shaft after the tip passes, as observed experimentally by Arshad et al. (2014) and Doreau-Malioche et al. (2018).

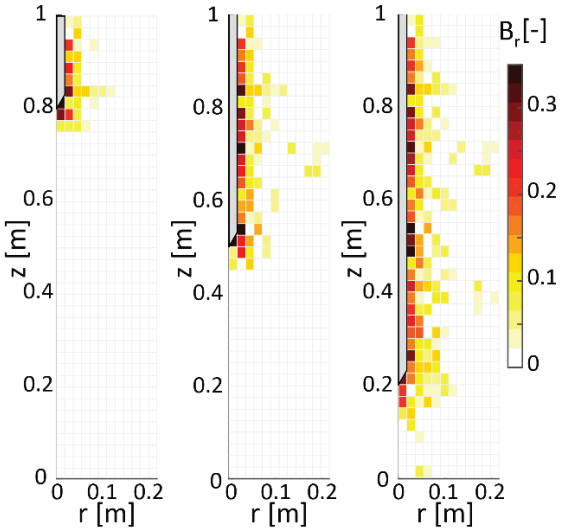

Figure 17 . DEM breakage distributions corresponding to three penetration depths.

The crushing profiles corresponding to three penetration depths are depicted in Figure 17, showing similar profiles to those obtained in crushable grain FEM analyses by Zhang et al. (2013). Both numerical approaches are in agreement with experiments reported by (Yang et al., 2010) and predict that the crushing-influenced zone is mainly confined close to the shaft.

Yang et al (2010) report that breakage ratios B_r=0.2 applied within their most highly crushed Zone 1, which extends over the $1< r/R <1.6$ range from the pile axis, with ratios of 0.09 and 0.07 ratios applying in their more distant Zones 2 and 3 respectively. The necessary particle scaling and the resulting limited number of particles make it difficult to distinguish such zones from the DEM analysis, as the sampling volumes are too small to give representative results. Nevertheless, analysis of Figure 17 shows average B_r ratios of 0.22 in the $1< r/R <2$ and 0.09 over the $2 < r/R < 3$ range that match the experimental findings. Zhang et al's (2014) continuum FEM simulation captures the spatially varying evolution of B_r better than the DEM treatment.

Galvis-Castro et al. (2019) suggested that any constant thickness of the crushed particle band width provides an indirect indication that particle crushing occurs mostly at, or below, the pile tip during installation. Comparing Figures 16 and 17 shows the DEM results supporting this hypothesis. We recognise, however, that Yang et al (2010) observed in their experiments that the crushed sand became concentrated into annular areas that adhered to the piles' shafts as penetration continued, forming 'crusts' whose thickness grew gradually with *h/R*. Yang et al (2010) argued that surface shear abrasion, which is not captured in the DEM analysis, fed this growth and note that similar 'fractured sand crusts' have been observed in the field around piles driven in sands. Yang et al (2010) and Jardine (2019) argue that such abrasion and the very large number of load cycles applied during field driving contribute to shaft radial stresses continuing to decay at larger *h/R* ratios than is expected by current FEM or DEM analyses.

4 CONCLUSIONS

DEM simulations offer new insights into the stress conditions developed around piles penetrating in sand. The analyses reported both match and help explore the pile calibration chamber experiments reported by Jardine et al. (2013a) and Yang et al. (2010). The crushable DEM model employed was calibrated to match element test conducted on the same NE34 Fontainebleau sand before being employed to study how grain crushing, and monotonic versus cyclic jacking, affected the micromechanical mechanisms that

give rise to key macro-scale features of pile behaviour. The main findings are:

1) Quasi-static DEM simulations indicated pile tip resistances q_c that followed similar profiles, independently of whether piles advanced by monotonic or cyclic jacking.

2) In line with recent experimental evidence (Doreau-Malioche et al., 2018; Mao et al., 2016) particle crushing occurred within a limited volume that extended to ≈ 4 radii below the pile base.

3) The degree of crushing predicted by the DEM model was broadly compatible with that observed experimentally. No crushing was predicted along the shaft, although it is recognised that surface abrasion may add to the thickness of any crushed sand crust seen in physical experiments or pile driving in the field.

4) The average stresses determined within volumes of the modelled soil particle arrays at given depths below the pile tip rose sharply as the tip approached from above, and declined sharply as it penetrated below to greater depth. They also varied with radial distance from the pile axis.

5) The DEM analysis predictions are broadly comparable to both the experimental observations and earlier independent FEM analyses undertaken with an advanced crushable soil model.

6) The DEM simulations show a strongly non-uniform stress regime developing around the pile shaft, with marked arching above the pile tip and stress maxima over the $2<r/R<6$ range that match the experiments, as interpreted by Jardine et al. (2013b). However, the DEM analysis indicates more clearly visible peaks in the vertical and circumferential stresses than were seen in the experiments, where the latter were harder to measure and therefore subject to greater scatter.

7) The penetration simulations identified key aspects of the stress paths provoked in the sand around the pile tip and shaft. The latter include large rotations of the principal stress axes (by as much as 250^0) during penetration as well extreme stress peaks as the tip arrives and decrease massively as it passes, leaving the sand mass around the shaft in a state of arching.

8) Arching was accentuated by grain crushing but did not appear to be as strongly influenced by cyclic changes in the jack's pile head loads.

9) Close similarities were noted between the directions of the principal strain axis directions observed experimentally by (Galvis-Castro et al. 2019) and the DEM model principal stress axis, showing an apparently nearly co-axial global material response in the sand.

10) The insights provided by the DEM into interparticle stresses, force chains and particle incremental displacements highlight how circumferential arching develops around the shaft through local unloading. Variations over time in such arching offers one potential explanation for the shaft capacity growth with age that occurs around industrial piles driven in sand.

5 ACKNOWLEDGEMENTS

This research was primarily supported by the first Author's Junior Research Fellowship at Imperial College. The BGA and the ISSMGE are also gratefully acknowledged for assisting with the first Author's travel and conference fees. Matteo Ciantia is particularly thankful to Professors A. Gens and M. Arroyo for many fruitful discussions and for their support on this research.

6 REFERENCES

Altuhafi, F.N., Jardine, R.J., Georgiannou, V.N., Moinet, W.W., 2018a. Effects of particle breakage and stress reversal on the behaviour of sand around displacement piles. *Géotechnique* **68**, 546–555.

Altuhafi, F.N., Jardine, R.J., Georgiannou, V.N., Moinet, W.W., Ciantia, M.O., Arroyo, M., Gens, A., 2018b. Effects of particle breakage and stress reversal on the behaviour of sand around displacement piles. *Géotechnique* 1–2 https://doi.org/10.1680/jgeot.18.D.010.

Arroyo, M., Butlanska, J., Gens, A., Calvetti, F., Jamiolkowski, M., 2011. Cone penetration tests in a virtual calibration chamber. *Géotechnique* **61**, 525–531.

Arshad, M.I., Tehrani, F.S., Prezzi, M., Salgado, R., 2014. Experimental study of cone penetration in silica sand using digital image correlation. *Géotechnique* **64**, 551–569.

Bolton, M.D., Gui, M.W., Garnier, J., Corte, J.F., Bagge, G., Laue, J., Renzi, R., 1999. Centrifuge cone penetration tests in sand. *Géotechnique* **49**, 543–552.

Boschi, K., di Prisco, C., Ciantia, M.O., 2019. Micromechanical investigation of grouting in soils. *Int. J. Solids Struct*. https://doi.org/10.1016/j.ijsolstr.2019.06.013.

Butlanska, J., Arroyo, M., 2015 Discussion of "Stresses Developed around Displacement Piles Penetration in Sand" by Z. X. Yang, R. J. Jardine, B. T. Zhu, and S. Rimoy. J. Geotech. Geoenvironmental Eng.**141**(3), 1-3.

Butlanska, J., Arroyo, M., Gens, A., (2009). *Homogeneity and Symmetry in DEM Models of Cone Penetration*. AIP Conf. Proc 425–428.

Butlanska, J., Arroyo, M., Gens, A., O'Sullivan, C., (2014). Multi-scale analysis of cone penetration test (CPT) in a virtual calibration chamber. *Can. Geotech. J.* **51**, 51–66.

Butlanska, J., de Toledo, M., Gens Solé, A., (2010). *Size effects on a virtual calibration chamber.* In: Seventh European Conference on Numerical Methods in Geotechnical Engineering. pp. 225–230.

Calvetti, F., (2008). Discrete modelling of granular materials and geotechnical problems. *Eur. J. Environ. Civ. Eng.* **12**, 951–965.

Carroll, R., Carotenuto, P., Dano, C., Salama, I., Silva, M., Gavin, K. and Jardine, R. 2019. Field experiments at three sites to investigate the effects of age on steel piles driven in sand. *Géotechnique*.

Christoffersen, J., Mehrabadi, M.M., Nemat-Nasser, S., 1981. A Micromechanical Description of Granular Material Behavior. *J. Appl. Mech.* **48**, 339.

Ciantia, M., Arroyo, M., Zhang, N., Emam, S., 2017. *Periodic cells for large-scale problem initialization*. In: EPJ Web of Conferences.

Ciantia, M.O., Arroyo, M., Butlanska, J., Gens, A., 2016. DEM modelling of cone penetration tests in a double-porosity crushable granular material. *Comput. Geotech.* **73**, 109–127.

Ciantia, M.O., Arroyo, M., Calvetti, F., Gens, A., 2015. An approach to enhance efficiency of DEM modelling of soils with crushable grains. *Géotechnique* **65**, 91–110.

Ciantia, M.O, Arroyo, M., O'Sullivan, C., Gens, A., 2019a. Micromechanical Inspection of Incremental Behaviour of Crushable Soils. *Acta Geotech.* 1–20. https://doi.org/10.1007/s11440-019-00802-0

Ciantia, M.O., Arroyo, M., O'Sullivan, C., Gens, A., Liu, T., 2019b. Grading evolution and critical state in a discrete numerical model of Fontainebleau sand. *Géotechnique* 1–15. https://doi.org/10.1680/jgeot.17.P.023

Ciantia, M.O., Boschi, K., Shire, T., Emam, S., 2018. Numerical techniques for fast generation of large discrete-element models. *Proc. Inst. Civ. Eng. - Eng. Comput. Mech.* **171**(4), 147–161.

Coetzee, C.J., 2019. Particle upscaling: Calibration and validation of the discrete element method. *Powder Technol.* **344**, 487–503.

Coop, M.R., Klotz, E.U., Clinton, L., 2005. The influence of the in situ state of sands on the load–deflection behaviour of driven piles. *Géotechnique* **55**, 721–730.

Doreau-Malioche, J., Combe, G., Viggiani, G., Toni, J.B., 2018. Shaft friction changes for cyclically loaded displacement piles: an X-ray investigation. *Géotechnique Lett.* **8**, 66–72.

Einav, I., 2007. Breakage mechanics—Part I: Theory. *J. Mech. Phys. Solids* **55**, 1274–1297.

Falagush, O., McDowell, G. R., Eng, C., Yu, H.-S., 2015. Discrete Element Modeling of Cone Penetration Tests Incorporating Particle Shape and Crushing. *I. J. Geomech.* **15**(6), 04015003

Galvis-Castro, A.C., Tovar-Valencia, R.D., Salgado, R., Prezzi, M., 2019. Effect of loading direction on the shaft resistance of jacked piles in dense sand. *Géotechnique* **69**(1)16–28.

Gens, A., Arroyo, M., Butlanska, J., Carbonell, J.M., Ciantia, M., Monforte, L., O'Sullivan, C., 2016. Simulation of the cone penetration test: Discrete and continuum approaches.

Aust. Geomech. J. **51**.
Gupta, R.C., 1991. Finite Strain Analysis for Deep Cone Penetration. *J. Geotech. Eng.* **117**, 1610–1630.
Huang, A.-B., Ma, M.Y., 1994. An analytical study of cone penetration tests in granular material. *Can. Geotech. J.* **31**, 91–103.
Huang, X., Hanley, K.J., O'Sullivan, C., Kwok, F.C.Y., 2014. Effect of sample size on the response of DEM samples with a realistic grading. *Particuology* **15**, 107–115.
Itasca, C.G.I., 2016. Particle Flow Code, V. 5.0.
Janda, A., Ooi, J., 2016. DEM modeling of cone penetration and unconfined compression in cohesive solids. *Powder Technol*. **293**, 60–8.
Jardine, R.J., Chow, FC, Overy, RF and Standing, J.R., 2005. *ICP design methods for driven piles in sands and clays*". Thomas Telford Ltd, London p. 105.
Jardine, R.J, Standing, J.R and Chow, F.C. 2006 Some observations of the effects of time on the capacity of piles driven in sand. *Géotechnique* **55**(4), 227-244
Jardine, R.J., Zhu, B.T., Foray, P., Yang, Z.X., 2013a. Interpretation of stress measurements made around closed-ended displacement piles in sand. *Géotechnique* **63**, 613–627.
Jardine, R.J., 2013. Advanced laboratory testing in research and practice. *2nd Bishop Lecture*. Proc. ICSMGE, Eds Delage et al., Presses des Ponts, Paris, Vol 1, pp. 35-55.
Jardine, R.J., Zhu, B.T., Foray, P., Yang, Z.X., 2013b. Measurement of stresses around closed-ended displacement piles in sand. *Géotechnique* **63**, 1–17.
Jardine, R.J., 2019. Geotechnics, Energy and Climate Change. 56th Rankine Lecture, *Géotechnique*.https://doi.org/10.1680/jgeot.18.RL.001
Jiang, M., Dai, Y., Cui, L., Shen, Z., Wang, X., 2014. Investigating mechanism of inclined CPT in granular ground using DEM. *Granul. Matter* **16**, 785–796.
Jiang, M.J., Yu, H.S., Harris, D., 2006. Discrete element modelling of deep penetration in granular soils. *Int. J. Numer. Anal. Methods Geomech.* **30**, 335–361.
Klotz, E.U., Coop, M.., 2001. An investigation of the effect of soil state on the capacity of driven piles in sands. *Géotechnique* **51**, 733–751.
Lade, P. V., Yamamuro, J.A., Bopp, P.A., 1996. Significance of Particle Crushing in Granular Materials. *J. Geotech. Eng.* **122**, 309–316.
Lehane, B.M., Schneider, J.A., Xu, X., 2005. A review of design methods for offshore driven piles in siliceous sand. UWA Rep. GEO 5358.
Lu, Q., Randolph, M.F., Hu, Y., Bugarski, I.C., 2004. A numerical study of cone penetration in clay. *Géotechnique* **54**, 257–267.
Luding, S., 2004. Micro–macro transition for anisotropic, frictional granular packings. *Int. J. Solids Struct.* **41**, 5821–5836.
Mao, W., Towhata, I., Aoyama, S., Goto, S., 2016. Grain crushing under pile tip explored by acoustic emission. *Geotech. Eng. J.* SEAGS AGSSEA 47.
Mao, W., Yang, Y., Lin, W., Aoyama, S., Towhata, I., 2018. High Frequency Acoustic Emissions Observed during Model Pile Penetration in Sand and Implications for Particle Breakage Behavior. *I. J. Geomech.* **18**(11), 04018143
McDowell, G.R., Falagush, O., Yu, H.-S., 2012. A particle refinement method for simulating DEM of cone penetration testing in granular materials. *Géotechnique Lett*. **2,** 141–147.
Muir Wood, D. 2007. The magic of sands – the 20th Bjerrum Lecture presented in Oslo, 25 November 2005. *Can. Geotech. J.* **44**(11), 1329–1350.
Monforte, L., Arroyo, M., Carbonell, J.M., Gens, A., 2017. Numerical simulation of undrained insertion problems in geotechnical engineering with the Particle Finite Element Method (PFEM). *Comput. Geotech.* **82**, 144–156.
Phuong, N.T.V., van Tol, A.F., Elkadi, A.S.K., Rohe, A., 2016. Numerical investigation of pile installation effects in sand using material point method. *Comput. Geotech.* **73**, 58–71.
Pournaghiazar, M., Russell, A.R., Khalili, N., 2013. Drained cavity expansions in soils of finite radial extent subjected to two boundary conditions. I*nt. J. Numer. Anal. Methods Geomech.* **37**, 331–352.

Quezada, J.C., Breul, P., Saussine, G., Radjai, F., 2014. Penetration test in coarse granular material using Contact Dynamics Method. *Comput. Geotech.* **55**, 248–253.

Rimoy, S., Silva, M., Jardine, R., Yang, Z.X., Zhu, B.T., Tsuha, C.H.C., 2015. Field and model investigations into the influence of age on axial capacity of displacement piles in silica sands. *Géotechnique* **65**, 576–589.

Russell, A.R., Muir Wood, D., 2009. Point load tests and strength measurements for brittle spheres. *I. J. Rock Mech. Min. Sci.* **46**, 272–280.

Russell, A.R., Muir Wood, D., Kikumoto, M., 2009. Crushing of particles in idealised granular assemblies. *J. Mech. Phys. Solids* **57**, 1293–1313.

Salgado, R., Mitchell, J.K., Jamiolkowski, M., 1998. Calibration Chamber Size Effects on Penetration Resistance in Sand. *J. Geotech. Geoenvironmental Eng.* **124**, 878–888.

Santamarina, J.C., 2003. *Soil Behavior at the Microscale: Particle Forces.* In: Soil Behavior and Soft Ground Construction. American Society of Civil Engineers, Reston, VA, 25–56.

Seif El Dine, B., Dupla, J.C., Frank, R., Canou, J., Kazan, Y., 2010. Mechanical characterization of matrix coarse-grained soils with a large-sized triaxial device. *Can. Geotech. J.* **47**, 425–438.

Sharif, Y., Brown, M., Ciantia, M.O., Knappett, J., Davidson, C., Cerfontaine, B., Robinson, S., 2019. *Numerically modelling the installation and loading of screw piles using DEM*. In: Davidson, et al. (Eds.), Proceedings of the 1st International Screw Pile Symposium on Screw Piles for Energy Applications. Dundee, 101-8.

Tehrani, F.S., Arshad, M.I., Prezzi, M., Salgado, R., 2018. Physical Modeling of Cone Penetration in Layered Sand. *J. Geotech. Geoenvironmental Eng.* **144**, 04017101.

Ting, J.M., Corkum, B.T., Kauffman, C.R., Greco, C., 1989. Discrete Numerical Model for Soil Mechanics. *J. Geotech. Eng.* **115**, 379–398.

Tran, Q.A., Chevalier, B., Breul, P., 2016. Discrete modeling of penetration tests in constant velocity and impact conditions. *Comput. Geotech.* **71**, 12–18.

Tu, F., Ling, D., Hu, C., Zhang, R., 2017. DEM-FEM analysis of soil failure process via the separate edge coupling method. *Int. J. Numer. Anal. Methods Geomech.* **41**, 1157–1181.

White, D., Bolton, M.D., 2004. Displacement and strain paths during plane-strain model pile installation in sand. *Géotechnique* **54**, 375-397.

White, D., Lehane, B.M., 2004. Friction fatigue on displacement piles in sand. *Géotechnique* **54**, 645–658.

Yang, Z.X., Jardine, R.J., Zhu, B.T., Foray, P., Tsuha, C.H.C., 2010. Sand grain crushing and interface shearing during displacement pile installation in sand. *Géotechnique* **60**, 469–482.

Yang, Z.X., Jardine, R.J., Zhu, B.T., Rimoy, S., 2014. Stresses Developed around Displacement Piles Penetration in Sand. *J. Geotech. Geoenvironmental Eng.* **140**, 04013027.

Zhang, C., Nguyen, G.D., Einav, I., 2013. The end-bearing capacity of piles penetrating into crushable soils. *Géotechnique* **63**, 341–354.

Zhang, C., Yang, Z.X., Nguyen, G.D., Jardine, R.J., Einav, I., 2014. Theoretical breakage mechanics and experimental assessment of stresses surrounding piles penetrating into dense silica sand. *Géotechnique Lett.* **4**,11–16.

Zhang, N., Arroyo, M., Ciantia, M., Gens, A., 2018. *DEM Investigation of Particle Crushing Effects on Static and Dynamic Penetration Tests*. In: Wu, W., Yu, H.-S. (Eds.), Proceedings of China-Europe Conf. on Geotech.Engineering. Springer, Cham, Vienna. 274–278.

Zhang, N., Arroyo, M., Ciantia, M.O., Gens, A., Butlanska, J., 2019. Standard penetration testing in a virtual calibration chamber. *Comput. Geotech.* **111**, 277–289.

Zhang, N., Evans, M., 2019. Discrete numerical simulations of torpedo anchor installation in granular soils. *Comput. Geotech.* **108**, 40–52.

Zhang, Z., Wang, Y.-H., 2015. Three-dimensional DEM simulations of monotonic jacking in sand. *Granul. Matter* **17**, 359–376.